ORIGINAL RESEARCH ARTICLE

Development of Cr and Al Pack Cementation Coatings on Co-Based γ/γ' Superalloys

TILL KÖNIG, S.P. HAGEN, S. VIRTANEN, and M.C. GALETZ

Co-based superalloys have been developed as candidate materials to replace Ni-based superalloys in hot sections of turbine engines, however, their oxidation resistance is limited. Therefore, in this work chromium and aluminum diffusion coatings were developed *via* the pack cementation process for novel γ/γ'-strengthened superalloys of the Co–Ni–Al–W system. This alloy system also offers the opportunity to vary the cobalt-to-nickel ratio and the tungsten content systematically to investigate their influence on the coating process. The coating process was shown to successfully enrich the surfaces of such alloys either in aluminum or chromium. For Al, the result was the formation of (Co, Ni)Al on top of an interdiffusion zone, while for chromium a Cr-rich layer in solid solution with the substrate along with the formation of σ-phase were observed. The coating formation mechanisms are discussed for both coatings in the light of activities and phase formation.

https://doi.org/10.1007/s11661-022-06807-x

I. INTRODUCTION

THE γ/γ'-strengthened Co-based superalloys have been developed as candidate materials to replace Ni-based superalloys in hot sections of turbine engines.[1–4] The efficiency of these engines is increased with higher gas temperature, which motivates research for materials with the capability to withstand higher temperatures over the past decades. In principle, the 40 °C higher melting temperature of Co compared to Ni should open the possibility for higher service temperatures of Co-based materials. In 2006[4] the γ'-phase in the Co–Al–W system was (re-)discovered, followed by the development of Co-based superalloys.[2] However, at temperatures beyond 900 °C the oxide scales on such systems grow faster than on Ni-based alloys with similar Al contents.[5] Generally, the ability to alloy such complex microstructural systems with Cr and Al is limited. Between this and the fact that even classical Ni-based superalloys cannot be used without coatings, the need for coating solutions for such Co-based superalloys is evident. For example, in the hottest sections of today's turbine engines the single crystal Ni-based superalloys, which are used for the blades, are equipped with a two-layered coating system.[6] Underneath the outer ceramic thermal barrier layer, bond coats are used to increase the oxidation, as well as corrosion resistance, and to avoid delamination of the outer layer.[7] Bond coats are either thermally sprayed MCrAlY coatings or Al diffusion coatings, which are made *via* the pack cementation process.[6] Cr diffusion coatings are also very interesting as they provide the best protection under hot corrosion conditions at intermediate temperatures up to 900 °C. They can be applied also *via* diffusion processes and are of importance for "colder turbine parts," such as blade roots.[8,9] The most common process to apply diffusion coatings is *via* a pack cementation process, which utilizes gaseous metal halides formed *in situ* by a halide activator (*e.g.*, NH_4Cl or $MnCl_2$) and the provided powder of the metal.[6] The metal halide decomposes at the surface of the alloy, depositing the metallic coating element while the halides are released to react again with the metal powder. After deposition, the respective metal (Al, Cr) interdiffuses with the alloy at the coating temperature (typically 700 °C to 1100 °C). Due to this diffusion the Al and Cr content is enriched also within the subsurface zone of the alloy.[9] For diffusion coatings, the morphology of the coating depends strongly on the substrate alloy and coating process parameters. For Al-based diffusion coatings generally high-activity and low-activity coatings are distinguished.[10] While the aluminide coating microstructures have been very well described for Ni-based alloys,[8,10] much less information can be found for Co-based alloys with Reference 11 being one of the few exceptions. For Cr diffusion coatings the available information is even rarer, with most of the

T. KÖNIG and M.C. GALETZ are with the High Temperature Materials, DECHEMA-Forschungsinstitut, Theodor-Heuss-Allee 25, 60486 Frankfurt, Germany. Contact e-mail: till.koenig@dechema.de S.P. HAGEN and S. VIRTANEN are with the Friedrich-Alexander Universität Erlangen-Nürnberg, 91058 Erlangen, Germany.
Manuscript submitted April 6, 2022; accepted August 19, 2022.
Article published online September 11, 2022

Table I. Nominal Compositions of the Alloys Tested in This Study (At. Pct)

Alloys	Co	Ni	Al	W	Cr	Ti	Ta	Si	Hf
ERBOCo-1	**44.5**	**32**	8	**5**	6	2.5	1.5	0.4	0.1
ERBOCo-1X	**32**	**44.5**							
ERBOCo-1-W	**45.66**	**32.84**	8	**3**	6	2.5	1.5	0.4	0.1
ERBOCo-1X-W	**32.84**	**45.66**							

Differences are highlighted in bold. Note the proportionate adaption of the Co and Ni contents in order to assure identical Co/Ni ratios of ERBOCo-1 and ERBOCo-1-W as well as of ERBOCo-1X and ERBOCo-1X-W

literature focusing on Fe-based systems. Hard metal mixtures of WC–Co were also chromized, but in such cases the resulting coating is dominated by carbide formation.[12] In the present study, pack aluminization and chromizing of four multinary γ/γ'-strengthened alloys based on the Co–Ni–Al–W sub-system were investigated, integrating the coating process into the standard heat treatment procedure that was recently recommended for these Co-rich alloys.[1,13] Furthermore, the chosen four superalloys allow exploration of the influence of the Co/Ni ratio (0.7 *vs.* 1.4) and the W content (5 *vs.* 3 at. pct) on the coating morphology.

II. EXPERIMENTAL

A. *Preparation of Specimens*

The substrate materials[1,13] utilized were the two γ/γ' alloys ERBOCo-1 (Co/Ni: 1.4) and ERBOCo-1X (Co/Ni: 0.7). Additionally, derivatives of these, containing a lower W content, ERBOCo-1-W and ERBOCo-1X-W were investigated. All 4 alloys were cast *via* Bridgman investment casting by the Institute of Metals Science and Technology (WTM, University of Erlangen-Nürnberg (FAU), Germany) as 12-mm-diameter single crystal rods. Their compositions are shown in Table I. The heat treatment procedure originally designed by Volz *et al.*[1] is provided in Table II. Since the coating process also requires high temperatures and in order to avoid an unwanted change in the substrate's microstructure during an additional heating step, the 1st aging step of the regular thermal treatment was used to determine the pack cementation parameters. The homogenization process was conducted as a whole rod prior to the preparation of the specimens. The single crystal rods were cut into coupons of 3 mm thickness and ground to a P1200 finish. The surfaces, which were investigated within the present study, had an intended (001) orientation. The 1st aging and coating step is described in the subsequent section. After removal from the pack setup, the 2nd aging step was done in Ar and 5 vol pct H_2 with a previous 150 C for 5 hours drying step, to minimize oxidation of the specimens during the process.

B. *Pack Cementation*

The pack cementation process was applied to enrich the specimen surfaces in either Cr or Al. Prior to the pack cementation process, the specimens were rinsed in deionized water and subsequently ultrasonically cleaned in acetone. The weight of the specimens was measured before and after the coating process with an analytical balance (Mettler Toledo XP205).

An overview of the coating process is given in Table III. The source of the coating element for the Al pack cementation was an Al–Cr master alloy. For the pack cementation, the source powder of the respective coatings ($Al_{60}Cr_{40}$: Reading Alloys, Inc., Cr: Alfa Aesar 99 pct), the activator (NH_4Cl: Honeywell 99.5 pct, $MnCl_2$: Merck > 97 pct), and the inert filler (Al_2O_3: Honeywell > 98 pct) were weighed using a balance (Mettler Toledo XS2002s). The source of the coating element and the inert filler were mixed in a turbula mixer for 30 minutes. The hygroscopic activators were added after the mixing procedure to avoid moisture uptake and the whole powder mixture was thoroughly mixed by hand. The specimens were placed in the powder mixture in Al_2O_3 crucibles, which were sealed with Al_2O_3 tiles. The sealed crucibles were placed in a tube furnace (quartz tube), which was three times evacuated and flushed with Ar. Before heating to the actual coating temperature, the furnace was kept at 150 °C for 5 hours in an Ar + 5 vol pct H_2 flow, to remove any moisture and to further reduce oxidation during the coating procedure. The heat treatment for coating formation was done according to the parameters in Table III. The samples remained within the powered off furnace for cooling down to room temperature.

C. *Microscopic Examination and Evaluation*

After the coating process, all specimens were weighed and X-ray diffraction (XRD; Bruker D8 Advance) patterns were taken. Cross sections of the specimens were obtained by conventional cutting, mounting in epoxy resin, grinding, and polishing procedures. The cross sections were examined using light microscopy, scanning electron microscopy [SEM; Hitachi Flex SEM 1000, Hitachi SU5000, both equipped with energy-dispersive spectroscopy (EDS)] and electron microprobe analysis (EPMA; JEOL JXA-8100).

III. RESULTS AND DISCUSSION

The thickness (definition exemplarily highlighted in Figures 2(a) and 8(a)) and weight changes during the pack cementation process of the Al and Cr coatings are shown in Figure 1. The thicknesses and weight gains correspond well with each other and the ratio of weight

gain to thickness was similar for the tested alloys (Al coatings: 1.3 to 1.4 g/cm^3; Cr coatings: 2.9 to 3.3 g/cm^3).

The thickness of the Al coatings depended strongly upon the alloy composition. The coatings were significantly thicker for the Ni-rich alloys, ERBOCo-1X and ERBOCo-1X-W, in comparison to the Co-rich alloys. Less pronounced but still clearly visible, the W-rich alloys, ERBOCo-1 and ERBOCo-1X, showed thicker Al coatings than the corresponding alloys with lower W contents, while the weight change of the ERBOCo-1-W was higher than the corresponding alloy with the higher W content. The weight change shown in Figure 1 represents only the weight change during the pack cementation process. During the final heat treatment step (see Table II), an additional weight gain (due to oxidation) was measured (varying between 0.07 and 0.11 mg/cm^2).

Table II. Heat Treatments of the Substrates

Annealing Step	Temperature (°C)	Time (h)
Homogenization	1280	8
1st Aging/Coating	1050	5
2nd Aging	900	16

The heating rate was 5 K/min (except for the aluminized specimens during the 1st aging/coating step, where the heating rate was 7 K/min).

A. *Al Coatings*

The backscattered electron (BSE) SEM images, element maps, and line scans of the Al coatings after the final heat treatment are shown in Figure 2. All coatings consisted of an outer Al_2O_3 scale (exemplarily marked as zone no. 1 in Figure 2(b)), a thin (Co, Ni)Al scale (zone no. 2 in Figure 2(b)), and a thick (Co, Ni)Al scale with precipitates (zone no. 3 in Figure 2(b)) and an interdiffusion zone (zone no. 4 in Figure 2(b)). The precipitates within the latter are enriched in Ta, W, Ti, Hf, and Cr. The presence of (Co, Ni)Al-β-phase was confirmed in the as-coated state and after the second heat treatment *via* XRD, where also the W structure was measured (see Figure 3). The change of color during the final heat treatment at 900 °C in the Ar + 5 vol pct H_2 atmosphere (see Figure 4) indicates that the Al_2O_3 scale had formed within this step. As the sample lay flat on an Al_2O_3 crucible, the bottom side (c) showed different colors after this heat treatment, while the top side (d)

Table III. Parameters of the Pack Cementation of Al and Cr

	Al Pack Cementation	Cr Pack Cementation
Source of Coating Element	10 wt pct Al–Cr (60 to 40 at pct)	10 wt pct Cr
Activator	2 wt pct NH_4Cl	2 wt pct $MnCl_2$
Inert Filler	88 wt pct Al_2O_3	88 wt pct Al_2O_3
Heat Treatment	1050 °C, 5 h, 7 K/min	1050 °C, 5 h, 5 K/min
Atmosphere	6 L/h Ar + 5 vol pct H_2	6 L/h Ar + 5 vol pct H_2

The coating deposition is part of the heat treatment described in Table II.

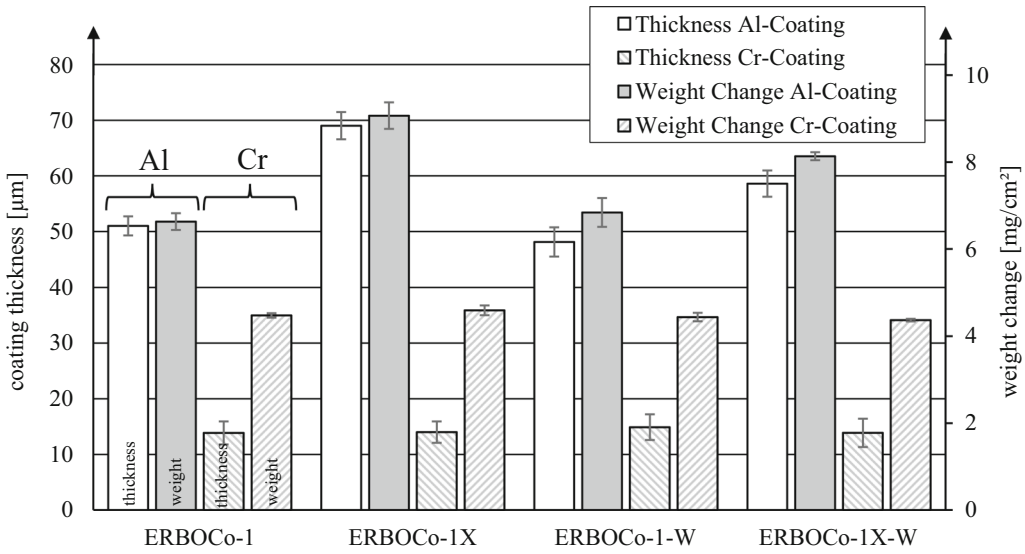

Fig. 1—Average coating thickness and weight changes of aluminized and chromized pack cementation coatings. Thicknesses were measured every 100 μm on stitched light microscope images with a 200 times magnification over a distance of at least 4 mm after the 2nd aging step. In contrast the weight changes, which were measured for three specimens per alloy, represent only the mass gain that is related to the 1st aging/coating step.

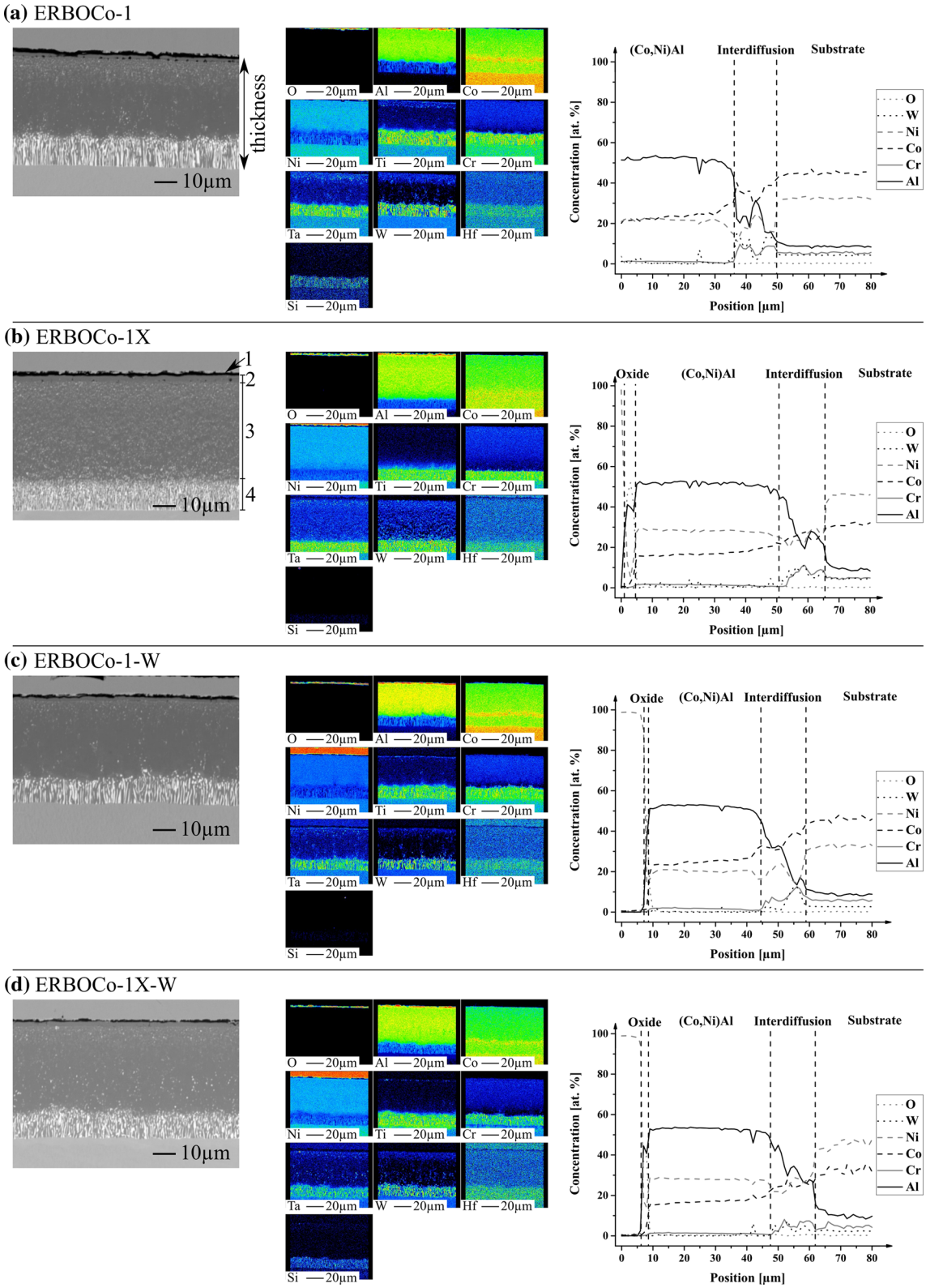

Fig. 2—BSE images, EPMA element maps, and EPMA line measurements of selected elements of (*a*) ERBOCo-1, (*b*) ERBOCo-1X, (*c*) ERBOCo-1-W, and (*d*) ERBOCo-1X-W with the Al pack cementation coating after the final heat treatment. The specimens have a Ni plating to protect the surface during preparation. The line measurements are performed from this plating ($x = 0\ \mu$) to the substrate nos. 1, 2, 3, and 4 in (b) refer to the oxide scale, outer and inner (Co, Ni)Al as well as the interdiffusion zone, respectively.

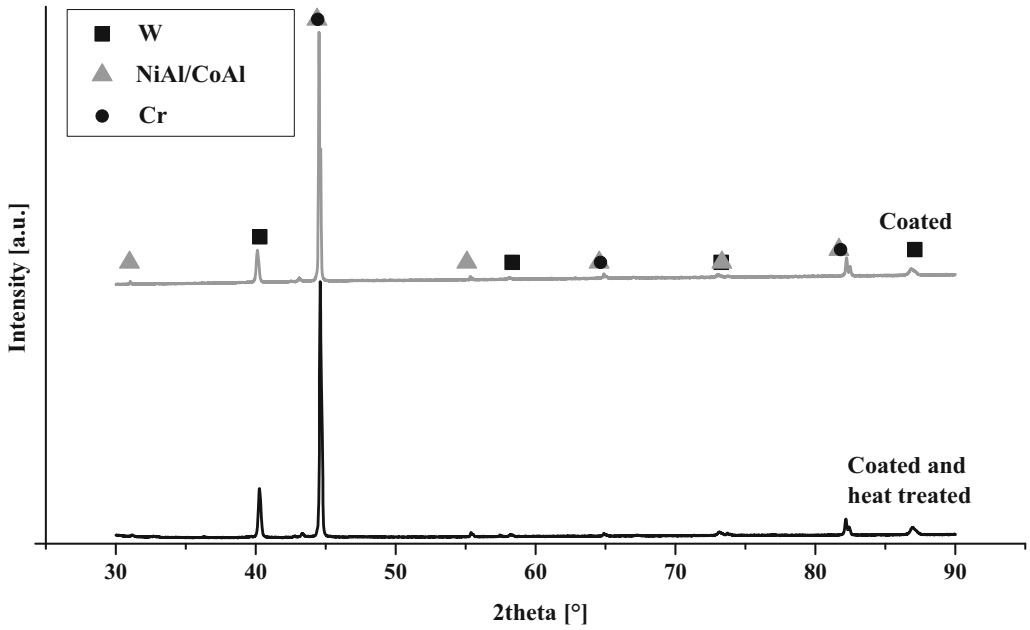

Fig. 3—Comparison of the XRD after Al pack cementation and the second heat treatment (16 h at 900 °C). Reference data taken from PDF2-1998: CoAl: 00-044-1115, NiAl: 00-044-1188, W: 00-004-0806.

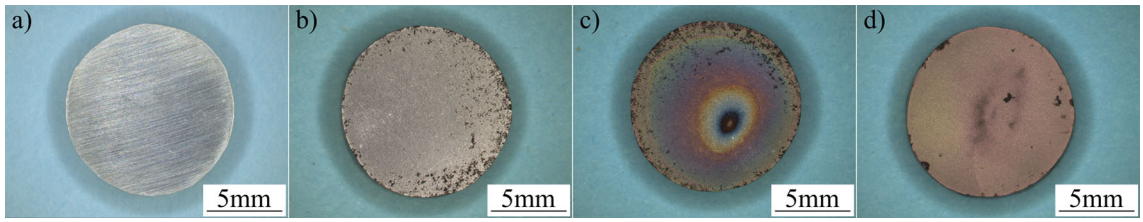

Fig. 4—Macroscopic images of the ERBOCo-1-W (*a*) cut and ground to a P1200 finish, (*b*) after Al pack cementation, bottom (*c*), and top side (*d*) after the final heat treatment.

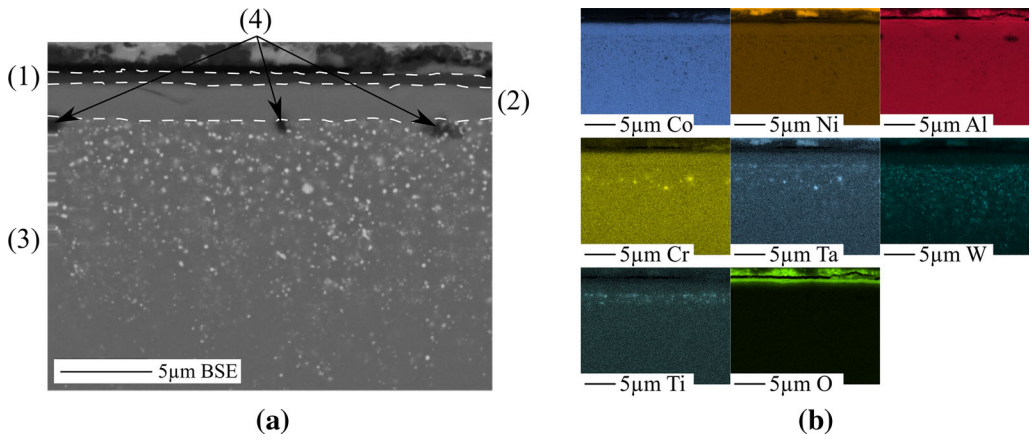

Fig. 5—BSE–SEM image (*a*) and EDS element maps (*b*) of the Al coating near the surface on the ERBOCo-1 alloy. The maps of the elements Si and Hf are not shown, since their content is below 1 at. pct. Si measurements are further interfered by W due to an overlap of the peaks. (1) Marks the oxide scale, (2) the precipitate-free (Co, Ni)Al, (3) the (Co, Ni)Al, and (4) porosity along the interface.

was homogenously colored. The oxidation during the final heat treatment is also shown in the more detailed EDS element maps in Figure 5 for the ERBOCo-1 alloy (note the crack between oxide scale and Ni plating) and corresponds well to the weight change during this step. Even though an Ar + 5 vol pct H_2 atmosphere was used, oxidation of Al during the heat treatment could not be prevented, due to the remaining oxygen

contamination of the atmosphere and the low dissociation pressure of Al_2O_3. The dark spots along the sample's margin are believed to be residual powder of the pack process.

The outermost zone underneath the oxide scale was an almost precipitate-free (Co, Ni)Al layer, which is exemplarily provided in Figure 5 no. 2 for ERBOCo-1 in higher magnification. For all samples, the line scans (Figure 2) suggest that the Co, Ni, and Al contents within this precipitate-free zone did not differ from the (Co, Ni)Al layer underneath. What is remarkable is the different ratios of Co/Ni, comparing the line scans of the (Co, Ni)Al layer in Figures 2(a) and (b) as well as Figures 2(c) and (d). In the Co-rich systems, Ni is present in the (Co, Ni)Al-phase of zone no. 3 in Figures 2(b) and 5 at a Ni/Co ratio of 1 (for 5 wt pct W) or close to 1 (for 3 wt pct W). But in the Ni-rich system, Ni is disproportionally enriched in the coating (up to 1.8 for both ERBOCo-1X and ERBOCo-1X-W). Further differences include for both W-rich alloys, ERBCo-1 and ERBOCo-1X, that the interface between the precipitate-free layer and the thicker (Co, Ni)Al layer was lined with Kirkendall pores (see Figures 2(a) and (b) as well as Figure 5 no. 4). The precipitates in the thick (Co, Ni)Al layer differed in their composition and size distribution. While a few large precipitates were formed that are considerably enriched in Cr and Ta, the smaller counterparts rather show above average W contents (see Figure 5 no. 3). Ti was observed near the surface in association with the W-rich precipitates. The amount and distribution of the precipitates differed depending on the alloy composition. As expected, the W-rich alloys ERBOCo-1 and ERBOCo-1X showed more precipitates in comparison to their corresponding alloys with lower W contents. The Ni-rich alloys showed a more uniform distribution and also more total precipitates in comparison to the alloys with a corresponding W content. At lower Ni content, all precipitates were observed especially near the specimens' surfaces, while generally the Cr- and Ta-rich precipitates were observed closer to the surface. Interestingly, the effect of the higher Ni content on precipitates is stronger than the effect of the higher W content and results in ranking, from higher to lower amounts (considering both small W- and large Cr–Ta-rich precipitates): (1) ERBOCo-1X, (2) ERBOCo-1, (3) ERBOCo-1X-W, (4) ERBOCo-1-W.

The interdiffusion zone still had a higher content of Al when compared to the substrate, but was additionally enriched in Ti, Ta, W, Cr, Hf, and Si. A detailed SEM image and EDS element maps of this area are shown in Figure 6 for the ERBOCo-1-W alloy, exemplarily. The interdiffusion zone showed columns of precipitates that were rich in W, Ta, and Cr. The line measurement in Figure 2 and also the element maps in Figure 6 show an increase in Co in the area of two phases.

B. *Cr Coatings*

In contrast to the Al coatings, the Cr coatings did not differ significantly in their thickness or weight change, as is shown in Figure 1 and they were thinner than the previously mentioned Al coatings. The Cr coatings consisted of multiple layers, whose individual thicknesses (Figure 7) and microstructures (Figure 8) are elucidated and discussed in the following.

The microstructures of the Cr pack coatings are shown in Figure 8. Similar to the thicknesses, the microstructures were only slightly affected by the alloy composition. The coatings consisted of an outer oxide layer rich in Cr and Mn. The latter was introduced due to the usage of $MnCl_2$ as an activator in the pack cementation process (the presence of Co or Ni could not be determined). On the surface an oxide with spinel structure was identified *via* Raman spectroscopy (Raman shift: ~ 685 cm^{-1}[14]). Similar to the aluminide coatings, a change in color during the final heat treatment step at 900 °C, exemplarily shown in Figure 9 (compare Figure 9(b) with (c)) for a ERBO-Co-1X specimen, indicates that this oxide has formed during the final annealing step at 900 °C, which is in line with a simultaneous, small weight gain (0.03 to 0.08 mg/cm^2). The subsurface zone was enriched in Cr with contents of around 50 to 60 at. pct and peaked beneath the oxide–metal interface at up to 80 at. pct. Two layers can be distinguished in the coating. The outer layer

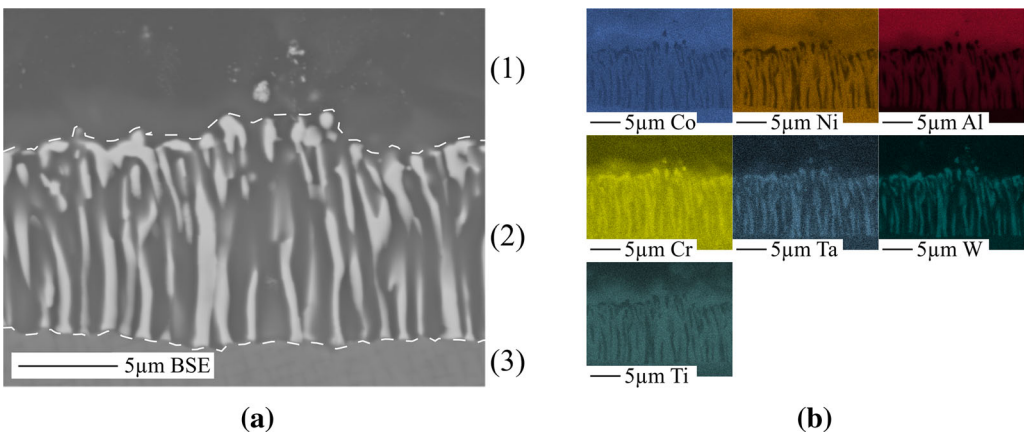

Fig. 6—BSE–SEM image (*a*) and EDS element maps (*b*) of the interdiffusion zone of the Al coating on the ERBOCo-1-W alloy. Interface are marked with a dotted line. (1) Shows the (Co, Ni)Al layer, (2) the interdiffusion zone, and (3) the substrate.

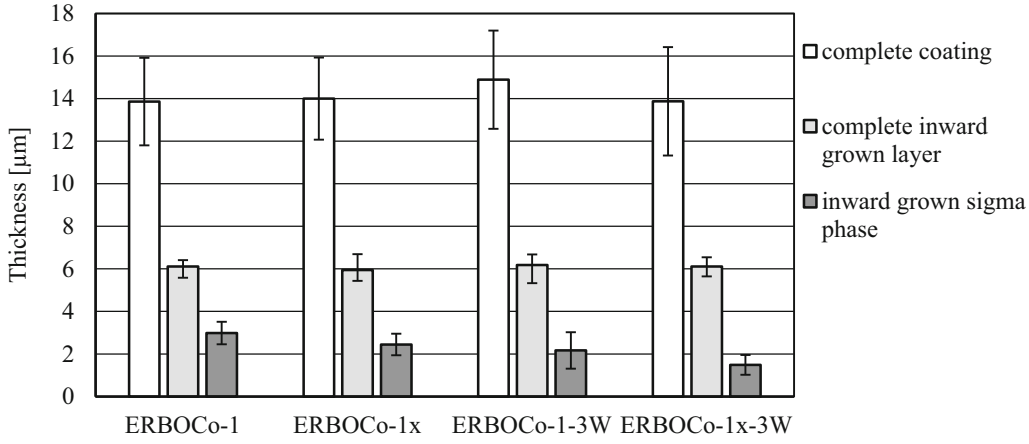

Fig. 7—Thicknesses of the Cr coatings and the comprising different layers (complete inward grown layer equals no. 4 to 6. in Fig. 10 and inward grown σ-phase no. 4). The overall coating thickness was measured based on optical microscope images as shown in Fig. 1. The thickness of the two layers were measured based on SEM images.

consisted of Cr, Co, and Ni, which had occasionally incorporated Al_2O_3 particles from the filler of the pack cementation process (see for example Figure 8(a)). This indicated an outward grown scale with small Al_2O_3 precipitates (see Figure 10 no. 2a). The Ni, Co, and Cr contents of the layer itself corresponded to the σ-phase, that is reported to have an approximate composition of xNi–(40 − x)Co–60Cr (x = 0 to 20).[15,16] In this layer, areas in contact with the oxide scale that were even richer in Cr were observed, which were most likely a solid solution of Cr and small amounts of Co, Ni, and Mn. The interface between the two layers was lined with small amounts of oxides and is believed to coincide with the initial surface (see no. 3 in Figure 10). The composition of the inner layer (no. 4 in Figure 10) corresponded again to σ-phase; however, it is believed to have grown by inward diffusion of Cr. Accordingly, no incorporated large Al_2O_3 particles were observed. Smaller Al_2O_3 precipitates were occasionally found, which likely formed during heat treatment and are not expected to be incorporated filler particles due to their smaller dimensions. W was found in both layers with an increasing content towards the substrate and a thin layer depleted in W was observed at the coating–substrate interface (see nos. 6 to 7 in Figure 10). The thickness ratio of the inner to the outer layer was the highest for the ERBOCo-1 alloy, followed by ERBOCo-1X, while the alloys with a low W content showed by far the smallest ratio (due to the thinnest inner layers).

Below this inward grown layer an interdiffusion zone (nos. 5 and 6 in Figure 10) with a decreasing Cr content in the through-thickness direction was found, whose width depended on the alloy composition. The thinnest interdiffusion zone was found for the ERBOCo-1 alloy, followed by the ERBOCo-1X. Both alloys with lower W content showed thicker interdiffusion zones (see Figure 7). This was the opposite trend to the thickness of the inward grown σ-phase and shows again the strong influence of the variance in composition on the diffusion mechanisms and growth of the different zones.

IV. DISCUSSION

A. *Al Coatings*

Al coatings are generally categorized according to the Al activity during the coating manufacturing process. One uses a high Al activity (most of the time pure Al) and a low temperature (below 900 °C), while the other uses a low Al activity (Al–Cr master alloys, Al content of up to 30 at. pct) at higher temperatures (1000 °C and higher).[9,11] According to the applied temperature of 1050 °C, the process utilized in this study can be considered a low activity pack cementation process (even if the Al content in the Al–Cr master alloy itself is rather high). The low Al activity pack cementation is reported to form an outward grown layer by diffusion of Ni or Co from the substrate into the coating, while the inward diffusion of Al is slower.[6,9]

For the analysis of the coating microstructure, it must be considered that the samples required a second heat treatment step (to adjust the γ–γ' microstructure), which also goes along with additional diffusion time without the supply of further Al *via* the gas phase. Still, some observations imply a dominantly inward grown coating, while others point towards an outward growth. For inward diffusion no incorporation of the pack powder, especially Al_2O_3 particles, into the coating would be expected. Such particles were not observed in the cross sections, but to a small extent in the macroscopic images in Figure 4 (dark spots). The second argument for an inward growth is that the (Co, Ni)Al layer matches the composition of a hyperstoichiometric β-phase after the second heat treatment (0.53 to 0.55 taken from the EPMA line scans *via* $\frac{c_{Al}}{c_{Al}+c_{Co}+c_{Ni}}$). The second heat treatment step (16 hours at 900 °C) results in further interdiffusion towards an equilibrium of the Al and Co/Ni activities between coating and substrate. Since no Al can be deposited from the gas phase, the Al content can be expected to decrease during the second heat treatment. However, no phase change by this heat treatment was observed in XRD measurements (see Figure 3). Therefore, an Al-rich (Co, Ni)Al scale must have been

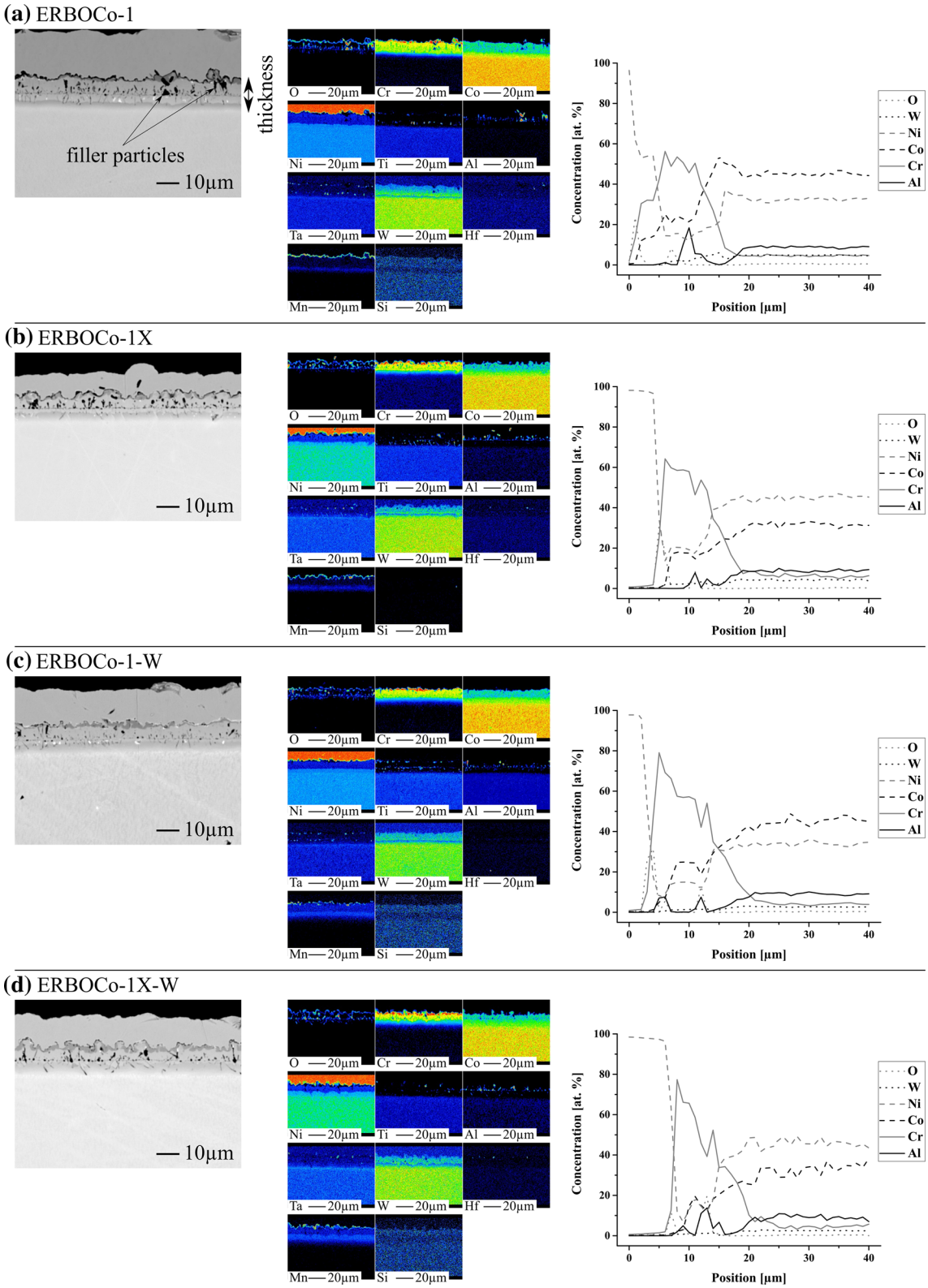

Fig. 8—BSE images, EPMA element maps, and EPMA line measurements of the alloys (*a*) ERBOCo-1, (*b*) ERBOCo-1X, (*c*) ERBOCo-1-W, and (*d*) ERBOCo-1X-W with the Cr pack cementation coating after the final heat treatment. The specimens have a Ni plating to protect the surface during preparation. The line measurements are performed from this plating to the substrate.

present before the second heat treatment as well. The ratio of the diffusion coefficients for Ni and Al in NiAl was measured by Shankar and Seigle[17] and depends on the stoichiometry of the intermetallic. The Al-rich (Co, Ni)Al implies a higher Al diffusion rate and therefore an inward grown coating, if further changes in diffusion by

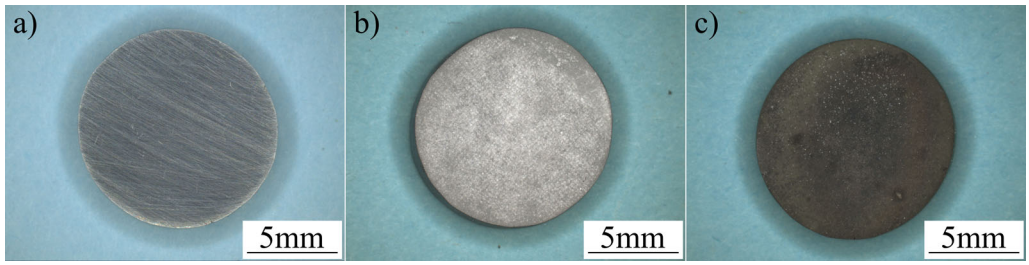

Fig. 9—Macroscopic images of an ERBOCo-1X specimen (*a*) cut and ground to a P1200 finish, (*b*) after Cr pack cementation, and (*c*) after the final heat treatment.

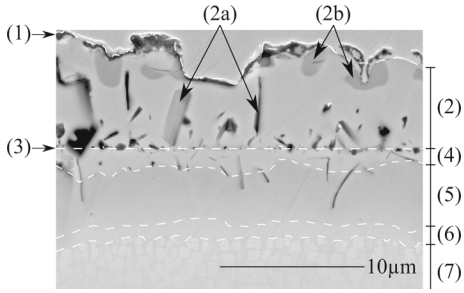

Fig. 10—BSE image of the Cr pack cementation coating on the ERBOCo-1X-W alloy after the final heat treatment. (1) Oxide scale, (2) outward grown σ-phase coating with (2a) Al_2O_3 inclusion/precipitates, (2b) Cr solid solution, (3) initial surface, (4) inward grown σ-phase coating, (5) interdiffusion zone, (6) interdiffusion zone with small precipitates, (7) substrate. Interfaces are marked with white dashed lines.

the replacement of Ni with Co in NiAl are neglected. Nevertheless, the huge difference between the elemental ratio of Co/Ni between the substrate and the coating suggests that outward diffusion of Ni still plays a significant role in the growth process, which is in line with the effect of this ratio on the coating thicknesses. The Ni-rich alloys ERBOCo-1X and ERBOCo-1X-W (Ni/Co ratio: 1.4) showed thicker coatings than the respective Co-rich alloys (Ni/Co ratio: 0.7). The influence of the higher Ni content in the alloy resulted also in a higher Ni content in the (Co, Ni)Al layer, formed by diffusion into the layer. Thus, the ratio of Ni to Co was around 1.7 to 1.9 in the layers developed on top of the Ni-rich alloys, while it was around 1 in the Co-rich alloys (see Figure 2). This demonstrates the selective enrichment of Ni, which cannot be solely explained by inward diffusion of Al. An outward grown coating appears also likely when considering the distribution of the other alloying elements, such as W, Ti, Ta, and Cr, whose diffusion has been shown to be comparably slow.[18–20] These elements are strongly enriched as topologically close-packed phases (tcp phases) in the interdiffusion zone, while a thin outer (Co, Ni)Al layer is completely free of precipitates and the main (Co, Ni)Al shows only fine precipitates. The enrichment of these elements in the interdiffusion zone is ascribed to the outward diffusion of nickel or cobalt, which results in the enrichment of Al below the initial surface until (Co, Ni)Al forms. The heavier elements precipitate, since they enrich as well and have a decreased solubility in the newly formed (Co, Ni)Al.[21] A (Co, Ni)Al coating, free of precipitates, is expected in this case, which is similar to the presented Al coatings shown in Figures 2 and 5. However, some fine precipitates are observed in the main (Co, Ni)Al layer. These fine precipitates can form during the second heat treatment step, since the solubility of the alloying elements in the β-phase decreases from 1050 °C (coating temperature) to 900 °C (heat treatment temperature).[22] Based on such considerations, outward growth of the coatings appears more likely, since the arguments for inward grown coatings are the absence of the expected incorporation of the pack powder into the coating and the diffusion data for pure NiAl.

The diffusion kinetics change very much for the different alloys, as demonstrated by the strong influence of the Ni/Co ratio on the coating thickness and composition. The W content was shown to influence the thickness of the Al coatings as well (see Figure 1). The coating thickness decreased along with the W content and the influence was more prominent on the Ni-rich alloys with a difference of about 10 μm, while it was only of 3 μm on the Co-rich alloys. Duret *et al.*[11] showed a decreased Al coating thickness on carbide-strengthened Co-based alloys due to the formation of tungsten carbide in the interdiffusion zone, which hindered outward diffusion of Ni and Co. The opposite was observed in the present case of the γ'-strengthened alloys, where the higher W content was associated with thicker coatings. Based on the ternary phase diagram of Ni–Al–W[23] it can be observed that an increase in W vastly enlarges the γ' area spreading into the γ solid solution area towards lower Al concentrations. This favors an earlier transition to the γ' phase at the Al diffusion front and a higher volume fraction of γ' in the interdiffusion zone. As the diffusion of Al in γ' is stated to be slower than in γ for a Ni- and a Co-based superalloy,[24] thinner Al diffusion coatings are expected at high W contents. Furthermore, W was shown to increase the Al activity in a Ni-based alloy,[25] which thereby decreases the Al activity gradient from the gas phase to the substrate. This gradient is the driving force for inward diffusion of Al and again thinner Al diffusion coatings would be expected on the alloys with high W content. Finally, a decrease of the diffusivity of Al was attributed to higher W contents in Ni–Al–Mo–W alloys,[26] which would further contribute to the trend

of thinner coatings on alloys with higher W content. Overall, the literature indicates several factors that should lead to a decreased coating thickness on ERBOCo-1 and ERBOCo-1X compared to the low W derivatives. The opposite is observed in the present study and is attributed to a significant part of the coatings being grown by Ni and Co outward diffusion. It is clear that the Co/Ni ratio has a much stronger effect than W when comparing the coating thicknesses in Figure 1.

B. *Cr Coatings*

Besides the industrial relevance and in contrast to the extensive work on Fe-based alloys,[27] microstructural descriptions of Cr coatings for Ni-based superalloys are rather rare in literature. For Ni-based alloys, Cr coatings are stated to be simpler than Al diffusion coatings, since Cr and Ni form only solid solutions and no additional intermetallic phases.[9] The morphology of a Cr pack cementation coating on pure Ni was described by Mazille[28] and Gaillard-Allemand *et al.*[29] to consist of two layers, with the outer being α-Cr and the inner γ-Ni, which was confirmed by the review of Bianco and Rapp.[9] Chang *et al.*[30] reviewed chromium diffusion coatings on Ni-based superalloys and, similarly, found them to consist of an (γ-Ni + α-Cr) layer and an outer α-Cr layer in the case of Cr-richer coatings. In the present study, σ-phase is additionally observed and replaces the α-Cr phase, which is only observed to a minor extent towards the surface. The existence of σ-phase can be directly linked to the presence of Co. While it does not occur in the binary Ni–Cr system, the σ-phase is well known in the ternary Co–Ni–Cr system.[16,31] The additional heat treatment (16 hours at 900 °C) must be mentioned as well, since the amount of α-Cr, which was formed by pack cementation, likely decreased during this step. During this heat treatment, the Cr was consumed on the one hand by the observed oxidation. On the other hand, additional diffusion time is provided without the supply of Cr, during which the Cr content in the coating leveled with the substrate and α-Cr likely dissolved to form additional σ-phase.

In contrast to the Al coatings, the observed microstructure and overall thicknesses of the Cr coatings were not influenced by the Co/Ni ratio or by the W content (see Figures 7 and 8). The phase composition of the inward grown part of the Cr coating changed slightly with the W content. The W-rich alloys, ERBOCo-1 and ERBOCo-1X, showed thicker layers of inward grown σ-phase, while the interdiffusion zone was thinner in comparison to the low W alloys. Even though this effect was small in relation to the standard deviation (see Figure 7), it is in line with the stabilization of the σ-phase towards lower Co contents by W.[32]

V. CONCLUSIONS AND OUTLOOK

In the present study, two diffusion coatings were developed on four new Co/Ni-based γ/γ′ superalloys using pack cementation processes that were in line with the required heat treatments. The surface of the alloys was successfully enriched either in Al, by the formation of (Co, Ni)Al, or in Cr, which led to σ-phase formation and Cr in solid solution within the alloy. For the aluminide coating, the W content and especially the Ni/Co ratio were observed to play a significant role in terms of growth mechanisms, and thus the coating thickness and size of the formed Al reservoir. In contrast, for the Cr coatings the thickness was not affected by the alloy composition. While the general morphology of both coatings is similar to those known for Ni-based superalloys, the influence of the described morphological differences on the oxidation and hot corrosion behavior needs to be evaluated in the future.

ACKNOWLEDGMENTS

The authors would like to thank Dr. Gerald Schmidt for conducting the EPMA measurements and Melanie Thalheimer for helping with SEM imaging and EDS measurements. Furthermore, we express our gratitude to Steffen Neumeier and Nicklas Volz as well as to Tobias Gaag for the valuable input regarding the derivatization of the original alloys and the casting of the single crystal ingots. Finally, scientific and financial support was provided by the Deutsche Forschungsgemeinschaft (DFG) through the Collaborative Research Center SFB-TR 103 (Project A5).

CONFLICT OF INTEREST

The authors declare that they have no conflict of interest.

FUNDING

Open Access funding enabled and organized by Projekt DEAL.

REFERENCES

1. N. Volz, C.H. Zenk, R. Cherukuri, T. Kalfhaus, M. Weiser, S.K. Makineni, C. Betzing, M. Lenz, B. Gault, S.G. Fries, J. Schreuer, R. Vaßen, S. Virtanen, D. Raabe, E. Spiecker, S. Neumeier, and M. Göken: *Metall. Mater. Trans. A*, 2018, vol. 49A, pp. 4099–4109.
2. A. Bauer, S. Neumeier, F. Pyczak, and M. Göken: *Scripta Mater.*, 2010, vol. 63, pp. 1197–1200.
3. E.T. McDevitt: *Mater. Sci. Forum*, 2014, vol. 783–786, pp. 1159–64.
4. J. Sato, T. Omori, K. Oikawa, I. Ohnuma, R. Kainuma, and K. Ishida: *Science*, 2006, vol. 312, pp. 90–91.
5. M. Weiser, M.C. Galetz, R.J. Chater, and S. Virtanen: *J. Electrochem. Soc.*, 2020, vol. 167, p. 21504.
6. M.C. Galetz: *Coatings for Superalloys*, IntechOpen, 2015. https://www.intechopen.com/citation-pdf-url/49100.
7. R. Darolia: *Int. Mater. Rev.*, 2013, vol. 58, pp. 315–48.
8. G.W. Goward and L.W. Cannon: *J. Eng. Gas Turbines Power*, 1988, vol. 110, pp. 150–54.
9. R. Bianco and R.A. Rapp: in *Metallurgical and Ceramic Protective Coatings*. K.H. Stern, ed., Chapman & Hall, London, 1996, pp. 236–60.
10. G.W. Goward and D.H. Boone: *Oxid. Met.*, 1971, vol. 3, pp. 475–95.
11. C. Duret, R. Mevrel, and R. Pichoir: in *Surface Engineering: Surface Modification of Materials*. R. Kossowsky and S.C. Singhal, eds., Springer, Dordrecht, 1984, pp. 452–68.
12. C.-L. Li, Y.-T. Lin, and J.-W. Lee: *Surf. Coat. Technol.*, 2009, vol. 204, pp. 1106–1111.
13. C.H. Zenk, N. Volz, C. Zenk, P.J. Felfer, and S. Neumeier: *Curr. Comput. Aided Drug Des.*, 2020, vol. 10, p. 1058.
14. Y. Chen, Z. Liu, S.P. Ringer, Z. Tong, X. Cui, and Y. Chen: *Cryst. Growth Des.*, 2007, vol. 7, pp. 2279–81.
15. X.L. Liu, G. Lindwall, T. Gheno, and Z.-K. Liu: *CALPHAD*, 2016, vol. 52, pp. 125–42.
16. T. Omori, J. Sato, K. Shinagawa, I. Ohnuma, K. Oikawa, R. Kainuma, and K. Ishida: *J. Phase Equilib. Diffus.*, 2014, vol. 35, pp. 178–85.
17. S. Shankar and L.L. Seigle: *Metall. Trans. A*, 1978, vol. 9, pp. 1467–76.
18. M. Karunaratne, D.C. Cox, P. Carter, and R.C. Reed: in *Superalloys 2000: Proceedings of the Ninth International Symposium on Superalloys*, September 17–21, 2000, Seven Springs, PA, T.M. Pollock, ed., The Minerals Metals & Materials Society TMS, Warrendale, PA, 2000, pp. 263–72.
19. M. Karunaratne and R.C. Reed: *Acta Mater.*, 2003, vol. 51, pp. 2905–19.
20. Y.M. Youssef, P.D. Lee, K.C. Mills, and R.C. Reed: *Mater. Sci. Technol.*, 2010, vol. 26, pp. 1173–76.
21. R. Pichoir and J.M. Hauser: *Environmental Degradation of High Temperature Materials: Spring Residential Conference*, Douglas, Isle of Man, 1980, 6/1–6/21.
22. C.C. Jia, K. Ishida, and T. Nishizawa: *Metall. Mater. Trans. A*, 1994, vol. 25A, pp. 473–85.
23. V. Raghavan: *J. Phase. Equilib. Diffus.*, 2009, vol. 30, pp. 281–82.
24. D. Kubacka, M. Weiser, and E. Spiecker: *Corros. Sci.*, 2021, vol. 191, p. 109744.
25. T. Galiullin, A. Chyrkin, R. Pillai, R. Vassen, and W.J. Quadakkers: *Surf. Coat. Technol.*, 2018, vol. 350, pp. 359–68.
26. G.H. Meier, F.S. Pettit, and A.S. Khan: *Rapid Solidification Processing, Principles and Technologies, III*, R. Mehrabian, ed., 1982, pp. 348–59.
27. A.R. Castle and D.R. Gabe: *Int. Mater. Rev.*, 1999, vol. 44, pp. 37–58.
28. H.M. Mazille: *Thin Solid Films*, 1980, vol. 65, pp. 67–74.
29. B. Gaillard-Allemand, M. Vilasi, T. Belmonte, C. Rives, T. Czerwiec, F. Belnet, O. Kerrec, and H. Michel: *MSF*, 2001, vol. 369–372, pp. 735–42.
30. J. Chang, Y. Li, H. Shi, L. Sun, and Y. Cui: *Proceedings of the 5th China Aeronautical Science and Technology Conference*, 1st ed., Springer, Singapore, 2022, pp. 861–70.
31. N. Zhao, W. Liu, J.-J. Wang, X.-G. Lu, and L. Zhang: *CALPHAD*, 2020, vol. 71, p. 101996.
32. P. Wang, B. Hu, X. Huang, and C. Zheng: *CALPHAD*, 2021, vol. 73, p. 102252.